PROCEEDINGS OF SCIENCE

VHE gamma-rays from the hyper-bright GRB 221009A: implications for external inverse-Compton and proton synchrotron emission

B. Theodore Zhang,[a,*] **Kohta Murase,**[b,c,d,e,a] **Kunihito Ioka,**[a] **Deheng Song,**[a] **Chengchao Yuan**[f] **and Péter Mészáros**[b,c,d]

[a] *Center for Gravitational Physics and Quantum Information, Yukawa Institute for Theoretical Physics, Kyoto University, Kyoto, Kyoto 606-8502, Japan*

[b] *Department of Physics, The Pennsylvania State University, University Park, PA 16802, USA*

[c] *Department of Astronomy & Astrophysics, The Pennsylvania State University, University Park, PA 16802, USA*

[d] *Center for Multimessenger Astrophysics, Institute for Gravitation and the Cosmos, The Pennsylvania State University, University Park, PA 16802, USA*

[e] *School of Natural Sciences, Institute for Advanced Study, Princeton, NJ 08540, USA*

[f] *Deutsches Elektronen-Synchrotron DESY, Platanenallee 6, 15738 Zeuthen, Germany*

E-mail: bing.zhang@yukawa.kyoto-u.ac.jp

The detection of the hyper-bright gamma-ray burst (GRB) 221009A provides an opportunity to investigate the nature of GRB emission and the origin of very-high-energy (VHE) gamma-rays. In this study, we examine the GeV-TeV emission within the framework of the external reverse-forward shock model. Motivated by observations from LHAASO, we aim to explain the multi-wavelength afterglow of GRB 221009A using a two-component jet model. Our analysis reveals that the energy spectra observed by LHAASO-WCDA exhibit dominance of the synchrotron self-component (SSC) from the narrow jet during the early phase. However, at later times, the proton synchrotron emission from the wide jet, accelerated in the reverse shock, becomes increasingly significant, which aligns with the observed spectral hardening. Furthermore, we observe that the external inverse-Compton mechanism, involving the upscattering of MeV gamma-rays by electrons accelerated at the external shock, is crucial in explaining the early emission in the range of approximately 1-200 GeV. This mechanism complements the synchrotron self-Compton component. Our results indicate the detectability of proton synchrotron emission from accelerated ultra-high-energy cosmic rays (UHECRs) and suggest that it could potentially account for the detection of photons at the $O(10\ \mathrm{TeV})$ level by LHAASO. Additionally, these findings may offer insights into constraining the mechanism responsible for UHECR acceleration.

38th International Cosmic Ray Conference (ICRC2023)
26 July - 3 August, 2023
Nagoya, Japan

*Speaker

PoS(ICRC2023)1460

1. Introduction

Very-high-energy (VHE) gamma-rays, with energies higher than $\sim$ 100 GeV, represent the most energetic segment of the electromagnetic (EM) spectrum. In the era of multimessenger astrophysics, the detection of VHE gamma-rays, alongside observations of multiwavelength EM radiation, neutrinos, cosmic rays, and gravitational waves, offers opportunities to probe the mechanisms behind high-energy astrophysical processes [e.g., 1].

Gamma-ray bursts (GRBs) rank among the most luminous explosions in the Universe [2]. In 2019, the detection of two TeV gamma-ray bursts (GRBs), GRB 190114C [3, 4] and GRB 180720B [5], opened a new window in the VHE band for studying GRBs and provided novel insights into their nature.

On October 9 2022, GRB 221009A was observed by the Fermi Gamma-Ray Burst Monitor (GBM) at T_0 = 13:16:59.99 UT. GRB 221009A is an extraordinarily bright and energetic GRB, with isotropic-equivalent energy of $\mathcal{E}_k \sim 3 \times 10^{55}$ erg (assuming a radiative efficiency of 10%) at a redshift $z = 0.15$ [6]. The *Fermi*-LAT detected gamma-rays with energies exceeding 100 MeV, with the highest-energy photon reaching 99.3 GeV. Notably, the Large High Altitude Air Shower Observatory (LHAASO) reported the detection of over 64,000 photons with energies above 0.2 TeV within the initial 3000 seconds [7], with the highest-energy gamma-ray recorded at 18 TeV [8].

The origin of VHE gamma-rays in GRBs has been extensively discussed in the context of the standard afterglow model, involving processes such as synchrotron self-Compton (SSC) or external inverse-Compton (EIC). Additionally, the synchrotron emission from ultra-high-energy (UHE) protons has been proposed as an alternative mechanism for generating VHE gamma-rays in GRBs. The proton synchrotron emission offers an advantage in producing gamma-rays above 10 TeV, a challenging range for the leptonic SSC and EIC processes due to the limitations imposed by the Klein-Nishina effect.

The detection of VHE gamma-rays through the proton synchrotron emission model in GRBs would provide strong evidence that GRBs are candidate sources of ultrahigh-energy cosmic rays (UHECRs). It has been proposed that the acceleration of UHECRs is possible in the internal shock model [e.g., 9, 10] or reverse shock model of GRBs [e.g., 11, 12], whereas the acceleration of UHECRs in the forward shock region via the diffusive shock acceleration mechanism is difficult due to the relatively weak magnetic field strength of the external medium. GRB internal shocks may occur at smaller radii, where the escape of gamma-rays above 10 TeV is challenging unless the Lorentz factor is exceptionally large. The observed prompt emission in the MeV band suggests that GRB 221009A is a long-lasting GRB, with a T_{90} duration of at least 600 seconds, indicating a scenario of a thick ejecta shell where the presence of a long-lasting reverse shock can be expected. In this study, we investigate the UHECR proton synchrotron emission process within the reverse shock model.

2. GeV - TeV gamma-rays from reverse shock

We analyze the data from *Fermi*-LAT collected between 203s and 1000s after the Fermi GBM trigger time (T_0) of 13:16:59.99 UT. The flux light curve can be seen in Fig. 1. We divide the analysis into three time intervals after T_0: 203s - 294s, 294s - 410s, and 410s - 1000s. However,

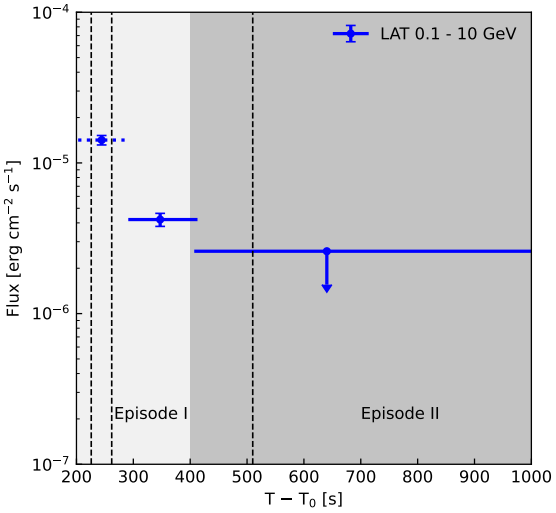

Figure 1: The flux light curve observed by the *Fermi*-LAT from $T_0 + 203$ s to $T_0 + 1000$ s is shown. The first time interval overlaps with the LAT Bad Time Interval due to photon pile-up and is included for reference purposes only. The black-dashed lines represent the three peak times of the prompt emission observed by Konus-Wind.

it's important to note that the first time interval coincides with the LAT Bad Time Interval due to photon pile-up. Therefore, we only include it for reference purposes. The analysis consists of two episodes. In the first episode (Episode I), the data is strongly influenced by the active prompt emission phase. In contrast, the second episode (Episode II) is considerably less affected by the prompt emission until the reverse shock completes its passage through the ejecta.

For simplicity, we assume that the ultrarelativistic thick ejecta moves into the external medium. Two types of shocks are formed: a reverse shock (RS), which propagates back into the ejecta shell and increases the internal energy, and a forward shock (FS), which moves into the external medium and energizes the swept-up matter. In the thick shell regime, the width of the ejecta, denoted as Δ, can be estimated as $\approx c\delta T \simeq 1.9 \times 10^{13}\ \delta T_{2.8}$ cm, where δT represents the duration of the GRB ejecta released by the source measured in the GRB frame. The typical time for the reverse shock to complete its crossing through the ejecta is around $t_\times \approx 0.71\delta T(1+z) \simeq 540\ \delta T_{2.8}$ s. The Lorentz factor of the shocked ejecta at the crossing radius $r_\times$ can be approximated as $\Gamma_\times \simeq 83\ \mathcal{E}_{k,55}^{1/8} n^{-1/8} \delta T_{2.8}^{-3/8}$ when measured in the stellar frame. The relative Lorentz factor, $\Gamma_{\rm rel}$, is approximately $0.5(\Gamma_\times/\Gamma_0 + \Gamma_0/\Gamma_\times) \simeq 1.7\Gamma_{0,2.4}$ in the frame of unshocked ejecta. The crossing radius of the reverse shock depends on the isotropic-equivalent kinetic energy $\mathcal{E}_k$ and density of the external medium $n_{\rm ex}$, $r_\times \simeq 3.8 \times 10^{17}\ \mathcal{E}_{k,55}^{1/4} n_{\rm ex}^{-1/4} \delta T_{2.8}^{1/4}$ cm. The magnetic field strength in the comoving frame can be estimated as $B_\times = [32\pi\epsilon_B n_{\rm ej} m_p c^2(\Gamma_{\rm rel}-1)(\Gamma_{\rm rel}+3/4)]^{1/2} \simeq 8.6\ {\rm G}\epsilon_{B,-1}^{1/2} \mathcal{E}_{k,55}^{1/4} \Gamma_{0,2.4}^{-1} \delta T_{2.8}^{-3/4} n^{1/4} (g(\Gamma_{\rm rel})/1.7)^{1/2}$, where ϵ_B represents the energy fraction of internal energy converted into the magnetic energy. The maximum energy of UHECR protons under the confinement condition satisfies $t_{\rm acc} < t_{\rm dyn}$, where $t_{\rm acc} = \eta t_L$ is the acceleration timescale, t_L is the Larmor time and $t_{\rm dyn} = R/\Gamma_{\rm rs}$ is the dynamical timescale. The maximum energy can be approximated as $E_{\rm max,dyn} \approx \eta^{-1} e B_\times r_\times \simeq 1.0 \times 10^{21}$ eV $\eta^{-1} \mathcal{E}_{k,55}^{1/2} \Gamma_{0,2.4}^{-1} \delta T_{2.8}^{-1/2} \epsilon_{B,-1}^{1/2} (g(\Gamma_{\rm rel})/1.7)^{1/2}$, where η is a coefficient which is ~a few in the Bohm limit. Although the maximum energy of UHECRs

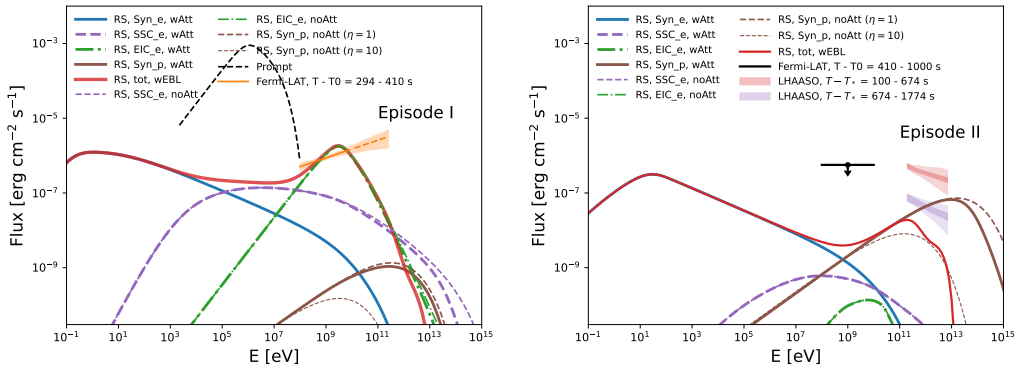

Figure 2: Multi-wavelength energy spectra up to the very-high-energy (VHE) range in our reverse shock model for Episode I and II. The corresponding physical parameters for Episode I are: $\Gamma_0 = 250$, $\mathcal{E}k = 1\times10^{55}$ erg, $n_{\rm ex} = 1$ cm^{-3}, $\delta T = 300$ s, $\epsilon_B^r = 0.05$, $\epsilon_e^r = 0.35$, $f_e^r = 0.8$, $s_e^r = 2.6$, $\epsilon_p^r = 0.1$, $s_p^r = 2.0$, $L_{\rm GRB}^{\rm iso}{}_\gamma = 2\times10^{52}$ erg s^{-1} . The corresponding physical parameters for Episode II are: $\Gamma_0 = 250$, $\mathcal{E}k = 2\times10^{55}$ erg, $n_{\rm ex} = 1$ cm^{-3}, $\delta T = 600$ s, $\epsilon_B^r = 0.5$, $\epsilon_e^r = 0.02$, $f_e^r = 0.01$, $s_e^r = 2.6$, $\epsilon_p^r = 0.08$, $s_p^r = 2.0$, $L_{\rm GRB}^{\rm iso}{}_\gamma = 2\times10^{50}$ erg s^{-1}.

may be limited by various energy cooling processes, such as synchrotron cooling, the production of UHECRs at the GRB reverse shock remains possible.

2.1 Upscattered prompt emission

Episode I undergoes significant influence from the active prompt emission phase. In the left panel of Fig. 2, we present the predicted energy spectrum within the reverse shock model for Episode I. The orange dashed region represents the average energy spectrum observed by *Fermi*-LAT between $T - T_0 = 294 - 410$ s, extrapolated to 300 GeV. The dot-dashed curve represents the upscattered prompt emission by non-thermal electrons accelerated in the reverse shock region during Episode I. This component dominates the energy flux beyond approximately 1 GeV. On the other hand, the dashed curve corresponds to the synchrotron self-component (SSC), which dominates the energy flux between 0.1 GeV and 1 GeV. It is important to note that the forward shock possesses a comparable energy to the reverse shock, suggesting its potential contribution to the GeV-TeV emission. The radiative process involving high-energy non-thermal electrons accelerated in the forward shock model may also be influenced by the prompt target photons.

2.2 Proton synchrotron emission

Episode II experiences significantly less influence from prompt emission until the reverse shock completes its passage through the ejecta. In the right panel of Fig. 2, we present the energy spectrum predicted for Episode II at the time of shock crossing, denoted as $t_\times$. Notably, the proton synchrotron emission can reach peak energies of approximately 10 TeV in the absence of extragalactic background light (EBL) absorption. Despite undergoing EBL-induced attenuation during propagation from the source to Earth, the harder spectral index enhances the proportion of approximately 10 TeV photons in the total observed gamma-ray spectrum. Additionally, we include the energy spectra measured by LHAASO-WCDA during two time intervals: $T - T_\star = 100 - 674$

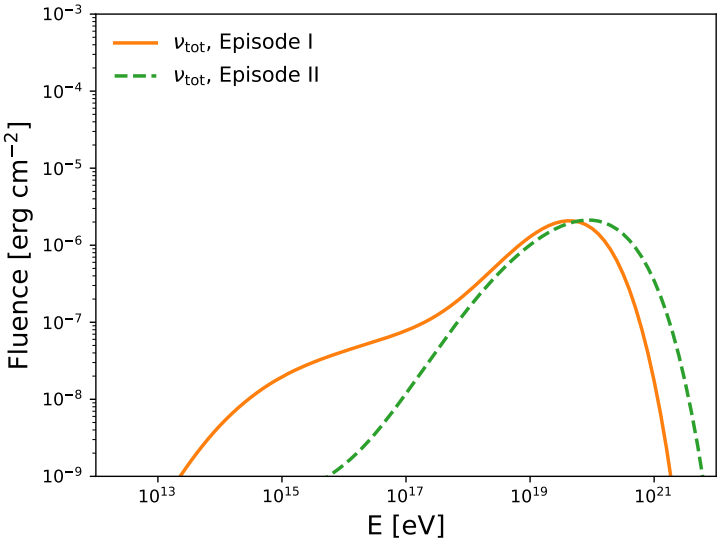

Figure 3: Neutrino fluences emitted during two time windows: 100 s (Episode I) and 300 s (Episode II).

s and $T - T_\star = 674 - 1774$ s. It is evident that the predicted flux during the shock crossing time aligns well with the energy flux measured by LHAASO-WCDA.

2.3 High-energy neutrino production

Fig. 3 displays the predicted neutrino fluences for Episode I and Episode II. In Episode I, the neutrino energy spectrum exhibits two distinct bumps. The first bump, peaking at around the PeV energy range, arises from the interaction between high-energy protons and prompt target photon fields through photomeson production. The second bump, with a peak energy at approximately 10 EeV, results from the interaction of ultra-high-energy (UHE) protons with lower-energy synchrotron photons emitted by the reverse shock. In contrast, the neutrino energy spectrum for Episode II displays a single bump, aligning with the assumption that the influence of prompt emission becomes less significant during this period.

3. Implications for LHAASO observations

LHAASO detected over 64,000 photons with energy larger than 0.2 TeV [7]. The VHE emission can be understood by considering a relativistic jet model with a core resembling a structured jet, characterized by a half-opening angle of approximately ~ 0.8 degrees. Motivated by the findings from LHAASO, we propose a two-component jet model. The narrow jet, akin to the core of a structured jet, possesses a higher Lorentz factor. Surrounding the narrow jet is a wider component that decelerates over time. To differentiate between the two jet components, we assume the narrow jet is dominated by magnetic energy, while the wide jet consists of matter dominated material. We set the start time of GRB ejecta at $T_\star = T - T_0 = 226$ s, as suggested by Ref. [7], which provides better accuracy when modeling the afterglow emission.

To conduct our calculations, we employ the Astrophysical Multimessenger Emission Simulator (AMES) code for numerical modeling of the GRB afterglow. To account for the impact of the reverse shock, we utilize the method proposed in [13, 14]. To determine the observed flux at a given observation time T, we integrate over the equal-arrival-time-surface (EATS). Furthermore, we consider the inluence of the jet break caused by the edge effect.

In Fig. 4, we present our results for fitting the energy spectra observed by LHAASO-WCDA using a two-component jet model. The dashed lines represent the SSC component from the narrow jet, which can explain the energy spectrum for all time intervals except the first interval $T - T_\star = 5 - 14$ s and the last two intervals $T - T_\star = 100 - 674$ s and $T - T_\star = 674 - 1774$ s. During the last two intervals, the predicted energy spectrum from the SSC component is steeper than the best-fit values due to the Klein-Nishina effect. The dotted-dashed lines represent the VHE gamma-rays produced by the proton synchrotron model from the matter-dominated jet, peaking at around 10 TeV. The two-component jet model provides a better fit to the observed energy spectrum by LHAASO. Futhermore, we observed that the energy flux around 0.2 TeV in the first time interval is difficult to explain with the SSC model, which peaks at higher energies, around a few TeV. It is possible that the excess of flux around 0.2 TeV in the earlier time interval can be explained by the EIC component, where prompt target photons are upscattered by non-thermal electrons accelerated in the external shock. This EIC component may account from the deficit in the observed flux at 0.2 TeV.

Fig. 5 presents the results of fitting the multi-wavelength afterglow of GRB 221009A using a two-component jet model. The model successfully explains the lightcurve across the X-ray to TeV range. The lightcurve generated by the proton synchrotron model is represented by dotted yellow lines, which aligns with a small flare occurring at $T_\star + [320, 550]$ s. However, explaining the afterglow lightcurve from radio to optical range solely with emission from the forward shock is challenging. It is likely that an additional component, such as emission from the reverse shock, is necessary [14].

4. Summary

In this study, we investigated the origin of VHE gamma-rays from GRB 221009A using the reverse shock model, which predicts the acceleration of non-thermal electrons and protons. Our findings demonstrate that both the forward shock and the reverse shock possess comparable energies, with the forward shock potentially contributing significantly to the VHE emission. However, while the forward shock can enhance the detection of gamma-rays around the TeV range by LHAAS, it faces challenges in explaining gamma-rays of approximately 10 TeV at later time. This highlights the significance of proton synchrotron emission from the reverse shock, as proposed in our research. Looking ahead, as the Cherenkov Telescope Array comes into play, we can anticipate the detection of more GRBs in the VHE gamma-ray range. Our work suggests that observing GRBs in this energy band could offer valuable insights into constraining the particle acceleration and radiative processes involving non-thermal electrons and protons in the reverse shock model.

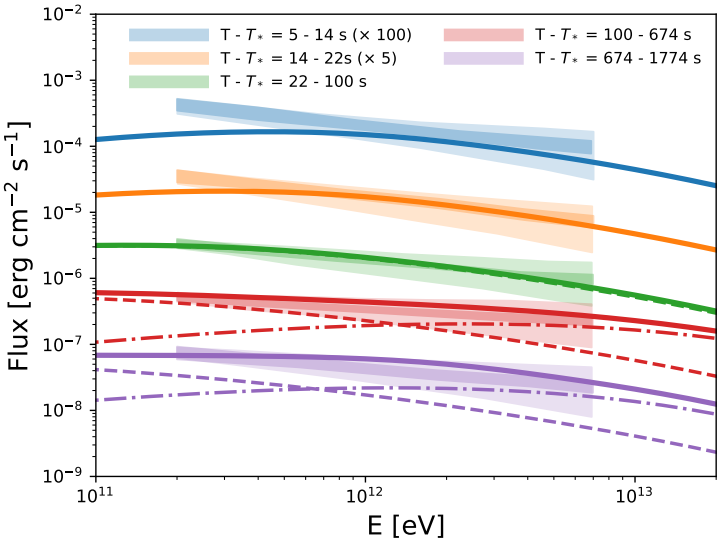

Figure 4: Energy spectra in the VHE range of GRB 221009A fitted with a two-component jet model. The dashed lines represent the energy spectra from the SSC component in the narrow jet, while the dotted-dashed lines depict the proton synchrotron emisison in the wide jet. The solid lines show the total emission combining both jet components. The corresponding physical parameters for the narrow jet are: $\Gamma_0 = 560$, $\mathcal{E}_k = 1.5 \times 10^{55}$ erg, $n_{\rm ex} = 1$ cm^{-3}, $\theta_j = 0.009$, $\delta T = 1$ s, $\epsilon_B = 6 \times 10^{-4}$, $\epsilon_e = 0.022$, $f_e = 1$, and $s_e = 2.6$. For the wide jet, the parameters are: $\Gamma_0 = 250$, $\mathcal{E}_k = 1. \times 10^{55}$ erg, $n_{\rm ex} = 1$ cm^{-3}, $\epsilon_B = 1 \times 10^{-4}$, $\epsilon_e = 0.006$, $f_e = 0.005$, $s_e = 2.6$, $\theta_j = 0.15$, $\delta T = 200$ s, $\epsilon_B^r = 0.7$, $\epsilon_e^r = 0.01$, $\epsilon_e^r = 1$, $\epsilon_p^r = 0.03$, and $s_p^r = 2.0$.

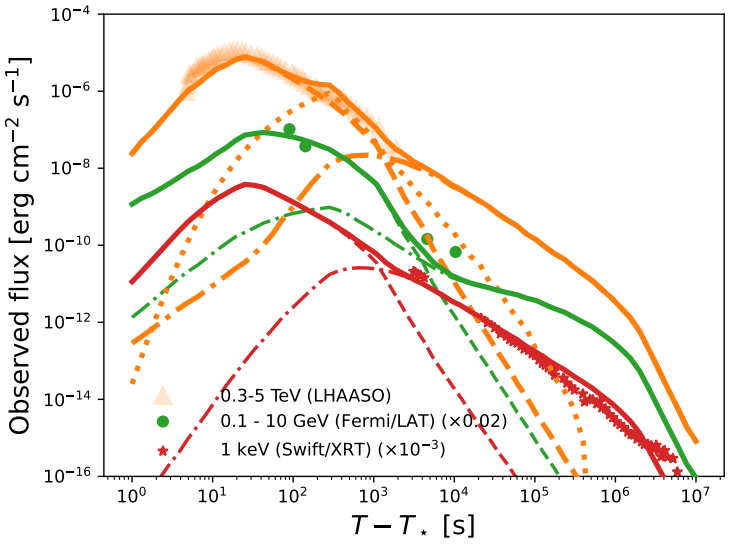

Figure 5: Multi-wavelength afterglow of GRB 221009A fitted with a two-component jet model, using the same physical parameters as in Fig. 4.

References

[1] K. Murase and I. Bartos, Ann. Rev. Nucl. Part. Sci. **69**, 477-506 (2019) doi:10.1146/annurev-nucl-101918-023510 [arXiv:1907.12506 [astro-ph.HE]].

[2] P. Meszaros, Rept. Prog. Phys. **69**, 2259-2322 (2006) doi:10.1088/0034-4885/69/8/R01 [arXiv:astro-ph/0605208 [astro-ph]].

[3] V. A. Acciari *et al.* [MAGIC], Nature **575**, no.7783, 455-458 (2019) doi:10.1038/s41586-019-1750-x [arXiv:2006.07249 [astro-ph.HE]].

[4] V. A. Acciari *et al.* [MAGIC], Nature **575**, no.7783, 459-463 (2019) doi:10.1038/s41586-019-1754-6 [arXiv:2006.07251 [astro-ph.HE]].

[5] H. Abdalla, R. Adam, F. Aharonian, F. Ait Benkhali, E. O. Angüner, M. Arakawa, C. Arcaro, C. Armand, H. Ashkar and M. Backes, *et al.* Nature **575**, no.7783, 464-467 (2019) doi:10.1038/s41586-019-1743-9 [arXiv:1911.08961 [astro-ph.HE]].

[6] D. Frederiks, D. Svinkin, A. L. Lysenko, S. Molkov, A. Tsvetkova, M. Ulanov, A. Ridnaia, A. A. Lutovinov, I. Lapshov and A. Tkachenko, *et al.* Astrophys. J. Lett. **949**, no.1, L7 (2023) doi:10.3847/2041-8213/acd1eb [arXiv:2302.13383 [astro-ph.HE]].

[7] Z. Cao *et al.* [LHAASO], Science **380**, 1390-1396 (2023) doi:10.1126/science.adg9328 [arXiv:2306.06372 [astro-ph.HE]]

[8] Huang Y., Hu S., Chen S., Zha M., Liu C., Yao Z., Cao Z., et al., 2022, GCN, 32677

[9] E. Waxman, Phys. Rev. Lett. **75**, 386-389 (1995) doi:10.1103/PhysRevLett.75.386 [arXiv:astro-ph/9505082 [astro-ph]].

[10] M. Vietri, Mon. Not. Roy. Astron. Soc. **278**, L1 (1996) doi:10.1093/mnras/278.1.L1 [arXiv:astro-ph/9510148 [astro-ph]].

[11] K. Murase, Phys. Rev. D **76**, 123001 (2007) doi:10.1103/PhysRevD.76.123001 [arXiv:0707.1140 [astro-ph]].

[12] B. T. Zhang, K. Murase, S. S. Kimura, S. Horiuchi and P. Mészáros, Phys. Rev. D **97**, no.8, 083010 (2018) doi:10.1103/PhysRevD.97.083010 [arXiv:1712.09984 [astro-ph.HE]].

[13] L. Nava, L. Sironi, G. Ghisellini, A. Celotti and G. Ghirlanda, Mon. Not. Roy. Astron. Soc. **433**, 2107 (2013) doi:10.1093/mnras/stt872 [arXiv:1211.2806 [astro-ph.HE]].

[14] R. Gill and J. Granot, doi:10.1093/mnrasl/slad075 [arXiv:2304.14331 [astro-ph.HE]].